

# **Systematic Assessment of Adsorption-Coupled Electron Transfer toward Voltammetric Discrimination between Concerted and Non-Concerted Mechanisms**

Donald C. Janda,<sup>a</sup> Kiran Barma,<sup>a,b</sup> Niraja Kurapati,<sup>a</sup> Oleksiy V. Klymenko,<sup>c,d</sup> Alexander Oleinick,<sup>c</sup> Irina Svir,<sup>c,e</sup> Christian Amatore,<sup>c,f</sup> and Shigeru Amemiya<sup>a,\*</sup>

<sup>a</sup> Department of Chemistry, University of Pittsburgh, 219 Parkman Avenue, Pittsburgh, Pennsylvania, 15260, United States

<sup>b</sup> UM-DAE, Centre for Excellence in Basic Sciences, University of Mumbai, Mumbai, 400098, India

<sup>c</sup> PASTEUR, Département de chimie, École normale supérieure, PSL Université, Sorbonne Université, CNRS, 75005 Paris, France

<sup>d</sup> Present address: Department of Chemical and Process Engineering, University of Surrey, Guildford GU2 7XH, United Kingdom

<sup>e</sup> Design Automation Department, Kharkiv National University of Radio Electronics, Nauky Avenue, 14, Kharkiv 61166, Ukraine

<sup>f</sup> State Key Laboratory of Physical Chemistry of Solid Surfaces, College of Chemistry and Chemical Engineering, Xiamen University, Xiamen, 361005, China

\* To whom all correspondence should be addressed. E-mail: [amemiya@pitt.edu](mailto:amemiya@pitt.edu). Fax : 412-624-8611.

Keywords: Adsorption-coupled electron transfer, Cyclic voltammetry, Kinetic zone diagram, KISSA-1D (Version 1.2.2c), COMSOL Multiphysics

## Abstract

The electron transfer and specific adsorption of a redox-active molecule are coupled in many important electrode reactions. Herein, we report a theoretical framework for the voltammetric discrimination of the concerted and non-concerted mechanisms of adsorption-coupled electron-transfer (ACET) reactions. In the concerted mechanism, an oxidant in the solution is simultaneously reduced and adsorbed to deposit a reductant on the electrode surface. Alternatively, electron-transfer and adsorption steps are mediated separately in the non-concerted mechanism. Our model involves the common adsorption step for both mechanisms to ensure consistent adsorption properties of the redox couple. For simplicity, we assumed a weak adsorption step that does not contribute to the current response. We predicted that not only a kinetically controlled adsorption step but also a chemically reversible electron-transfer step is required for the voltammetric identification of the reaction mechanism. High scan rates were required during cyclic voltammetry (CV) for the kinetic control of the adsorption step. Unique CV shapes, or characteristic changes therein, were expected for each mechanism during the reversible adsorption of oxidants or reductants. We modelled the reversible adsorption of both the oxidant and reductant for the reduction of benzyl chloride at a Ag electrode. The experimental CV of this chemically irreversible ACET reaction kinetically controlled the adsorption step but was consistent with either mechanism to quantitatively validate our model. A voltammetric discrimination of the concerted and non-concerted mechanisms has not been demonstrated, but it will be possible if both requirements are satisfied.

## 1. Introduction

Many important electrode reactions involve adsorption-coupled electron transfer (ACET), as defined by [1]



where O is an oxidant dissolved in the solution and  $R_{ads}$  is a reductant, R, adsorbed specifically on the electrode surface. The adsorbate is a ubiquitous and crucial intermediate or a product of electrocatalysis [2-4], photo-electrocatalysis [2], electrodeposition [5], electro-intercalation [6], and electro-polymerisation [7]. The mechanism of ACET reactions is not fully understood [1], despite their significance in both applied and fundamental electrochemistry. A concerted mechanism, which involves a simultaneous electron transfer (ET) and adsorption, is the only possible mechanism when O is not adsorbed and R is irreversibly adsorbed (Case I, Table 1). A non-concerted mechanism, which involves separate ET and adsorption steps, is also possible when O or R is reversibly adsorbed (Cases II and III, respectively). Important examples of the respective cases include electrodeposition with  $O = H^+$  [8] and  $Li^+$  [9] and electrocatalysis using  $R = O_2^{2-}$  [10] and  $CO_2^{2-}$  [11].

Herein, we propose the general requirements and experimental approaches for the voltammetric discrimination of concerted and non-concerted ACET reaction mechanisms. We have systematically assessed all possible adsorption scenarios to identify new concerted mechanisms (Cases II, III, and IV in Table 1). These concerted mechanisms involve the adsorption step required by their non-concerted counterparts to ensure consistent adsorption properties of the redox couples in the two mechanisms. The concerted mechanisms with the adsorption step yield more diverse sets of cyclic voltammograms (CVs) than those with only the ACET step (Case I) [1, 12, 13]. There has been a pioneering study on the possibility of voltammetric discrimination of these two mechanisms [1], wherein, for reasons unrelated to the present study, the mechanisms were compared on the basis of different adsorption properties of

the redox couples. A common adsorption step was not considered in the cited study [1], and the concerted mechanism of Case I was compared with the non-concerted mechanism of Cases II or III.

In this study, we have extended the diffusion-reaction model [1] to simulate the CVs of the ACET reactions for both the concerted and non-concerted mechanisms with a common adsorption step (Table 1). In our model, the ACET step (Equation 1) can be coupled with the reversible adsorption of the oxidant (Case II) or reductant (Case III), as follows:



The non-concerted mechanisms were modelled by coupling the respective adsorption steps with an inner-sphere [1, 14-17] or outer-sphere [1, 18, 19] ET for the non-ACET steps as follows:



The concerted mechanism, with a reversible adsorption of both the oxidant and reductant (Case IV), involved an additional ACET step, as follows [20, 21]:



The resultant scheme is hourglass-shaped, in contrast to the square scheme of the non-concerted counterpart based on the inner-sphere and outer-sphere ET steps [15, 22-27].

Our model can aid the experimental assessment of real ACET reactions via both the concerted and non-concerted mechanisms. Case II represents the electrodeposition of hydrogen atoms, that is, the Volmer reaction, and metal atoms, where the non-concerted mechanism was predicted theoretically [28, 29]. However, therein the experimental voltammograms were interpreted exclusively by considering the concerted mechanism of Case I [12, 13, 30], thereby eliminating any potential role of the adsorbed oxidants [8]. Case III represents the adsorption-coupled oxidation of ferrocene derivatives at highly

oriented pyrolytic graphite (HOPG) [31, 32]. Therein, the non-concerted mechanism agreed with the experimental CVs to account for the rapid kinetics of the outer-sphere ET step by the Marcus theory [33]. However, the CVs were not compared with those of a concerted mechanism [34]. Moreover, the non-concerted mechanism of Case IV was modelled for the voltammetric discrimination of the inner-sphere and outer-sphere ET steps [24, 27] to elucidate the inner-sphere and outer-sphere reduction of benzyl chloride at a Ag electrode by CV [26]. The non-concerted mechanism was also supported by density functional theory (DFT) [35], but it was not compared with the concerted mechanism.

We implemented the boundary conditions associated with Equations 1–6 in the diffusion-reaction model [1] to predict the voltammetric features that are unique to either of the concerted or non-concerted mechanisms. This prediction implied that the two mechanisms were voltammetrically discriminable when the common adsorption step was kinetically controlled [1] and the ET steps were chemically reversible. The unique voltammetric features were predicted by assuming a weak adsorption of O in Case II, R in Case III, or both in Case IV. Therefore, we neglected the current response based on a partial charge transfer through the formation of a chemical bond between the adsorbate and the electrode surface [36, 37]. The current response based on only ET steps (Equations 1 and 4–6) in our model was consistent with the experimental CVs at scan rates of up to 500 V/s [26]. The transient CVs agreed with the non-concerted mechanism [26] as well as the concerted mechanism to validate our model. For a quantitative analysis, the background current was recorded after the iR drop had been compensated for and deducted, to distinguish between the Faradaic and capacitive currents [38–40].

## 2. Model

### 2.1. Current Responses Based on the ET Steps

We simulated the current response based on the ACET and non-ACET steps to determine the unique voltammetric features of the concerted and non-concerted mechanisms, respectively. Our model neglected the current response based on a partial charge transfer [36, 37], a change in the double-layer capacitance, and the iR drop [41, 42]. The Faradaic CV was obtained by cancelling the iR drop through electronic feedback to subtract the capacitive current [38-40]. A Faradic CV can be obtained using macro-electrodes at low scan rates (<10 V/s) and micro-electrodes at high scan rates (>10 V/s) [26], which increase the current response.

For the concerted mechanisms of Cases II and III, the current response,  $i_{\text{et}}$ , was defined as follows:

$$i_{\text{et}} = -FAv_C^0 \quad (7)$$

where the reduction current has a negative sign [43],  $A$  is the electrode surface area, and  $v_C^0$  is the rate of the ACET reaction shown in Equation 1. The current response based on the non-concerted counterparts was given by

$$i_{\text{et}} = -FA(v_{\text{IS}}^{0\text{ads}} + v_{\text{OS}}^0) \quad (8)$$

where  $v_{\text{IS}}^{0\text{ads}}$  and  $v_{\text{OS}}^0$  are the rates of the inner-sphere (Equation 4) and outer-sphere (Equation 5) ET reactions, respectively.  $v_{\text{OS}}^0 = 0$  in Case II, and  $v_{\text{IS}}^{0\text{ads}} = 0$  in Case III. The current response for Case IV was defined by Equations S-26 and S-27, as described in the Supplementary Materials. The normalised current response,  $I$ , was defined as [1]

$$I = i_{\text{et}} \frac{RT}{F^2 v A \Gamma_s} \quad (9)$$

where  $v$  is the scan rate and  $\Gamma_s$  is the total surface concentration of the adsorption sites. For simplicity, we assumed equivalent adsorption sites for all species.

## 2.2. Diffusion-Reaction Model

We simulated the current response for the concerted or non-concerted mechanism by numerically solving the diffusion-reaction model [1]. Our model has been described in the Supplementary Materials, including Table S-1 for the definitions of all symbols and Tables S-2 and S-3 for the boundary conditions. A numerical solution was obtained by employing the finite element method in COMSOL Multiphysics [31, 32] (version 5.6, COMSOL, Burlington, MA). Since these simulations involve acute and challenging numerical problems, we ensured that the results obtained using COMSOL agreed with those obtained using the finite difference method implemented in the KISSA-1D software [1, 44] (version 1.2.2c). Moreover, we analytically verified the characteristic peak and limiting currents of the simulated CVs (see Tables S-4 and S-5).

We employed the previously reported diffusion-reaction model [1] but selected the appropriate boundary conditions associated with Equations 1–6. The diffusion equation for species  $i$  ( $= O$  or  $R$ ) was given by

$$\frac{\partial c_i}{\partial t} = D \left( \frac{\partial^2 c_i}{\partial x^2} \right) \quad (10)$$

where  $c_i$  is the concentration of species  $i$  at a distance  $x$  from the electrode surface and at time  $t$ , and the diffusion coefficients of the oxidant and reductant are both assumed to be  $D$ . Equation 10 describes the planar diffusion of the redox couple for a transient CV at the macroscopic electrodes at low scan rates ( $<10$  V/s) [45]. As demonstrated in the study cited in [26], planar diffusion based on Equation 10 is valid for microelectrodes when high scan rates ( $>10$  V/s) are used to obtain transient CVs [46]. Transient conditions are considered to emphasise the adsorption effects (see Equation 17).

Our model neglects adsorbate–adsorbate interactions for simplicity and defines the adsorption rate,  $v_{\text{ads}}^i$ , of a species  $i$  as [1]

$$v_{\text{ads}}^i = k_{\text{ads}}^i c_i \Gamma_M - k_{\text{des}}^i \Gamma_i \quad (11)$$

where  $k_{\text{ads}}^i$  and  $k_{\text{des}}^i$  are the adsorption and desorption rate constants, respectively;  $c_i$  and  $\Gamma_i$  are the concentrations of species  $i$  at the outer and inner Helmholtz planes, respectively; and  $\Gamma_M$  is the concentration of free adsorption sites. A Langmuir isotherm is obtained using  $v_{\text{ads}}^i = 0$  in Equation 11 to define the equilibrium constant,  $\beta_i$ , as

$$\beta_i = \frac{k_{\text{ads}}^i}{k_{\text{des}}^i} \quad (12)$$

Without adsorbate–adsorbate interactions, the rates of the ACET steps (Equations 1 and 6) are given by [1]:

$$v_C^0 = k_{\text{red}}^0 c_O \Gamma_M \exp \left[ -\frac{\alpha F}{RT} (E - E_{\text{app}}^0) \right] - k_{\text{ox}}^0 \Gamma_R \exp \left[ \frac{(1-\alpha)F}{RT} (E - E_{\text{app}}^0) \right] \quad (13)$$

$$v_C^{O_{\text{ads}}} = k_{\text{red}}^{O_{\text{ads}}} \Gamma_O \exp \left[ -\frac{\alpha F}{RT} (E - E_{\text{app}}^{O_{\text{ads}}}) \right] - k_{\text{ox}}^{O_{\text{ads}}} c_R \Gamma_M \exp \left[ \frac{(1-\alpha)F}{RT} (E - E_{\text{app}}^{O_{\text{ads}}}) \right] \quad (14)$$

where  $k_{\text{red}}^j$  and  $k_{\text{ox}}^j$  ( $j = O$  or  $O_{\text{ads}}$ ) are the reduction and oxidation rate constants, respectively;  $\alpha$  is the transfer coefficient, which is assumed to be 0.5;  $E$  is the electrode potential; and  $E_{\text{app}}^j$  is the apparent formal potential. The true formal potentials are defined by Equations S-10 and S-14.

In addition, the rates of the non-ACET steps (Equations 4 and 5) are given by the Butler-Volmer model as [1]

$$v_{\text{IS}}^{O_{\text{ads}}} = k_{\text{IS}}^{0,O_{\text{ads}}} \left\{ \Gamma_O \exp \left[ -\frac{\alpha F}{RT} (E - E_{\text{IS}}^{0',O_{\text{ads}}}) \right] - \Gamma_R \exp \left[ \frac{(1-\alpha)F}{RT} (E - E_{\text{IS}}^{0',O_{\text{ads}}}) \right] \right\} \quad (15)$$

$$v_{\text{OS}}^0 = k_{\text{OS}}^{0,0} \left\{ c_O \exp \left[ -\frac{\alpha F}{RT} (E - E_{\text{OS}}^{0',0}) \right] - c_R \exp \left[ \frac{(1-\alpha)F}{RT} (E - E_{\text{OS}}^{0',0}) \right] \right\} \quad (16)$$

where  $k_{IS}^{0,0_{ads}}$  and  $k_{OS}^{0,0}$  are the standard rate constants of the inner-sphere and outer-sphere ET steps, respectively, and  $E_{IS}^{0',0_{ads}}$  and  $E_{OS}^{0',0}$  are the formal potentials of the respective ET steps. Adsorbate–adsorbate interactions were neglected for simplicity while defining the inner-sphere ET rate (Equation 15).

### 2.3. Kinetic Zone Diagrams

Kinetic zone diagrams were developed for Cases II and III (see Tables S-4–S-7) to determine the experimental conditions required for the voltammetric discrimination of the concerted and non-concerted mechanisms. The key experimental conditions are represented by two dimensionless parameters of the common adsorption step. These parameters had been previously used to obtain the kinetic zone diagrams for the concerted mechanism of Case I and the non-concerted mechanism of Case II [1].

A dimensionless parameter,  $\kappa$ , represents the ratio of the peak current of an electrochemically reversible adsorption wave to that of an electrochemically reversible diffusion wave. Specifically,

$$\kappa = \frac{\Gamma_s}{c_0} \sqrt{\frac{Fv}{RTD}} \quad (17)$$

where  $c_0$  is the bulk oxidant concentration. A larger  $\kappa$  value corresponds to a higher dominance of the adsorption wave. For instance,  $\kappa$  increases with a higher scan rate and with a lower concentration of the redox-active molecule in a solution to enhance the adsorption effect.

The other dimensionless parameter,  $\lambda_{des}^i$ , represents the desorption rate constant normalised against the inverse of the CV time scale, as given by

$$\lambda_{des}^i = k_{des}^i \frac{RT}{Fv} \quad (18)$$

This parameter is equivalent to the ratio of the normalised adsorption rate constant,  $\lambda_{\text{ads}}^i$ , to the normalised strength of the interactions between the adsorbate and the electrode surface,  $\rho_i$ , with

$$\rho_i = c_0 \beta_i \quad (19)$$

where  $\lambda_{\text{des}}^i = \lambda_{\text{ads}}^i / \rho_i$ . The  $\lambda_{\text{ads}}^i / \rho_i$  ratio had been employed in a previous study to obtain kinetic zone diagrams [1]. In this study, a  $\rho_i$  value was specified for each kinetic zone diagram.

#### 2.4. Model Validation

Our model had been proven in previous studies, as well as the present study, to quantitatively account for experimental results from real ACET reactions. These results include experimental CVs of benzyl chloride at a Ag electrode (Case IV) via the non-concerted mechanism [26] and the concerted mechanism in this study. Our model was also validated by the CV of ferrocene derivatives at HOPG (Case III) via the non-concerted mechanism [31, 32] and the concerted mechanism discussed in this study. Interactions among adsorbates were determined by implementing the Frumkin isotherm in our model to quantitatively simulate the experimental CVs of some ferrocene derivatives at HOPG (Case III) [31, 32]. The model based on the Frumkin isotherm was also validated via voltammetric studies of ACET reactions using scanning electrochemical microscopy (SECM). These SECM studies include the electrodeposition of hydrogen (Case I) [47] and magnetite (Case III) [48] and the ACET reaction of cobalt complexes (Case III) [49]. All validation studies using our model confirmed that the interaction of the adsorbate with the electrode surface was potential-independent. More specifically,  $k_{\text{ads}}^i$ ,  $k_{\text{des}}^i$ , and  $\beta_i$ , were independent of the electrode potential, as assumed in this study.

### 3. Results and Discussion

#### 3.1. Requirements for Voltammetric Discrimination of Concerted and Non-Concerted Mechanisms

We assessed the ACET and non-ACET rates (Equations 13–16) analytically to conclude that concerted and non-concerted mechanisms can be discriminated voltammetrically when two requirements are satisfied: a kinetically controlled adsorption step, as proposed previously [1], and a chemically reversible ET step, as discovered in this study. If one of the requirements is not satisfied, the ACET step of the concerted mechanism becomes kinetically equivalent to the non-ACET step of the non-concerted counterpart, and the two corresponding mechanisms cannot be distinguished voltammetrically. The correspondence between the equivalent ACET and non-ACET steps has been summarised in Table 2, which also lists the required conditions. The equivalence was maintained under all mass-transport conditions, that is, at any concentration of a species near or at the electrode. The equivalence was derived by considering the equilibrium of the common adsorption step or the chemical irreversibility of the ET steps (see Supplementary Materials and Table S-8). The equivalences were kinetic, but consistent with the thermodynamic equivalence between the concerted and non-concerted mechanisms (Table S-9). The equivalences that included the outer-sphere ET step also required a low coverage of the electrode surface with the adsorbates, that is,  $\Gamma_M \approx \Gamma_s$ , in Equations 13 and 14 for the ACET steps.

Here, we discuss how the rates of the ACET and non-ACET steps paired with the adsorption step (Table 1) become equivalent (Table 2). Equivalence based on equilibrium adsorption is independent of the electrochemical or chemical reversibility of paired ET steps. In Case II, the paired ET steps yielded the adsorbed form of the reductant from the adsorbed and non-adsorbed forms of the oxidant. In Case III, both forms of the reductant were produced from the non-adsorbed form of the oxidant. When the adsorption steps were equilibrated dynamically, it was obscured which form of the oxidant in Case II (or

the reductant in Case III) contributed to the current response. Accordingly, discrimination between the ACET and non-ACET steps and, subsequently, between the corresponding mechanisms, was prevented.

When paired ET steps are only oxidative or reductive, owing to irreversible chemical reactions, equivalence is expected without the need for equilibrium adsorption. In Case II, the first-order oxidation rate of the ACET step (Equation 13) matched the first-order inner-sphere oxidation rate (Equation 15). In Case III, the reduction rate of the ACET step (Equation 13) was approximated to the first order, with  $\Gamma_M \approx \Gamma_s$ , to agree with the first-order outer-sphere reduction rate (Equation 16).

An analytical assessment of Case IV demonstrated that each mechanism involves two ET steps to yield ET equivalence for each pair of ACET and non-ACET steps (Table 2). Equivalence is achieved when the adsorption step maintains an equilibrium or the ET steps are either oxidative or reductive. All ET steps can be equivalent when the adsorption of both the oxidant and reductant maintains an equilibrium.

A formal potential is not useful for the discrimination of concerted and non-concerted mechanisms whose gross reactions are thermodynamically equivalent. The corresponding equivalences among the formal potentials of the ACET and non-ACET steps have been described in the Supplementary Materials (Table S-9). A formal potential is defined as the thermodynamic parameter of each ET step (Equations 13–16; see also Equations S-10 and S-14). The formal potential of an ACET (or non-ACET) step can be determined from the peak potential of the experimental CV by considering the concerted (or non-concerted) mechanism [1]. However, the formal potential can be expressed using the formal potential of the non-ACET (or ACET) counterpart (Table S-9) owing to the thermodynamic equivalence between their mechanisms.

### 3.2. ACET with Reversible Adsorption of Oxidant (Case II)

When the oxidant was reversibly adsorbed on the electrode surface (Case II), the ACET reactions were prominent, as exemplified by the electrodeposition of hydrogen and metal atoms. Molecular dynamics simulations and DFT have been combined to predict the non-concerted mechanism of hydrogen [28] and silver [29] electrodeposition. Small oxidant ions are strongly solvated, but specifically and weakly adsorbed on the electrode surface without significantly losing the solvation energy to mediate the inner-sphere ET step. However, experimental voltammograms have been interpreted predominantly by considering the concerted mechanism of Case I [12, 30]. Accordingly, the dependence of the electrodeposition kinetics on the electrode material has been attributed to the specific adsorption of only the reductants, as indicated by the volcano plot of hydrogen electrocatalysis. It is unclear whether weakly adsorbed oxidants can act as the true reactants in the inner-sphere ET step of the non-concerted mechanism [8].

#### 3.2.1. Kinetic Zone Diagrams

Kinetic zone diagrams resulting from the finite-element simulation of the CVs for Case II emphasise the differences between the concerted and non-concerted mechanisms (Figures 1A and 1B, respectively). The kinetic zone diagrams predict the possibility of a voltammetric discrimination of the two mechanisms as well as Cases I and II. The kinetic zone diagrams were plotted against  $\lambda_{\text{des}}^{\text{O}}$  and  $\kappa$  to represent four major kinetic zones: A, D, Kin, and KinD [1]. D and A represent the diffusion-controlled and adsorptive behaviour, respectively, and Kin represents a forward (or reverse) wave controlled purely by adsorption (or desorption) kinetics. Each zone covers reversible and irreversible ET kinetics, as indicated by R (or O) for reversible (or ordinary) kinetics and I for irreversible kinetics. Boundaries

were defined between the kinetic zones by analytically evaluating the characteristic peak and limiting currents of the reversible CVs (Tables S-4–S-7).

Kinetic diagrams were obtained for the weak adsorption of the oxidant with  $\rho_0 = 10^{-4}$  to avoid interference with reductant adsorption. However, the weak adsorption of the oxidant significantly affected the ability of the concerted mechanism to produce not only the AR/AI and DO/DI zones, which are expected only for the ACET step, but also the KinR/KinI and KinDR/KinDI zones, which are not expected for only the ACET step (Case I) and have been previously attributed only to the non-concerted mechanism [1]. Our diagram of the non-concerted mechanism is consistent with those developed previously [1], including all previously reported representative CVs [14-17]. In addition, our diagram includes the KinR'/KinI' zone, which is characteristic of a non-concerted mechanism (Figure 1B).

Kinetic zone diagrams confirmed the results of the analytical assessment of ACET and non-ACET kinetics (entry 1 in Table 2) for the voltammetric discrimination of concerted and non-concerted mechanisms. In particular, different CVs were expected for the two mechanisms with the same combination of adsorption parameters for a  $\lambda_{\text{des}}^0$  sufficiently small to kinetically control the common adsorption step. The AR/AI and DO/DI zones of the concerted mechanism (below the dotted line and boundary 4 in Figure 1A) partially correspond to the other zones of the non-concerted mechanism (Figure 1B). Moreover, the KinDR/KinDI zone of the concerted mechanism corresponds to the KinR/KinI zone of the non-concerted mechanism (below the dotted line in Figure 1B). In contrast, the concerted and non-concerted mechanisms are equivalent and indistinguishable in parts of the AR/AI, DO/DI, and KinR/KinI zones, where  $\lambda_{\text{des}}^0$  is sufficiently high to maintain the adsorption equilibrium. These regions are located above boundary 3 and the dotted line in Figure 1A and above boundaries 4 and 5 and the dotted line in Figure 1B.

### 3.2.2. Discrimination between Concerted and Non-Concerted Mechanisms

Our simulation results indicate that concerted and non-concerted mechanisms can be discriminated in Case II by analysing the transition between the common kinetic zones. For instance, identical transitions are expected at scan rates unique to each mechanism. The scan rate can be increased to observe the transition of the non-concerted mechanism from the AR/AI to the KinDR/KinDI zone. This transition has been indicated by a diagonal arrow across boundary **5** in Figure 1B. The corresponding transition in the concerted mechanism required a much larger increase in the scan rate. Moreover, the non-concerted mechanism transitioned from the DO/DI to the KinDR/KinDI zone at a higher scan rate (diagonal arrow across boundary **4** in Figure 1B). The same transition required a lower concentration of the oxidant for the concerted mechanism (lateral arrow across boundary **4** in Figure 1A). In contrast, a lower concentration of the oxidant changed the non-concerted mechanism from the KinDR/KinDI zone to the DO/DI zone (lateral arrow across boundary **4** in Figure 1B). Furthermore, a lower scan rate involved the transition of the concerted mechanism from the KinDR/KinDI to the KinR/KinI zone (diagonal arrow across boundary **3** in Figure 1A). This transition required a higher scan rate and passed through the KinR/KinI' zone in the non-concerted mechanism (diagonal arrows across boundaries **3** and **6** in Figure 1B).

The CV simulation for Case II also indicated that the non-concerted mechanism can be identified by the unique shape of the CVs in the KinR'/KinI' zone. Previously, the KinR'/KinI' zone was included in the KinR/KinI zone because both zones were expected for the non-concerted mechanism but not for the concerted mechanism without the adsorption step [1]. We considered the two zones to be distinct because the KinR/KinI zone was also expected for a new concerted mechanism with a common adsorption step. In the KinR'/KinI' zone, the sharp bell-shaped forward peak corresponded to the inner-sphere ET step, followed by the limiting current for the steady-state adsorption of the oxidant. In

contrast, a broad forward peak overlapped with the limiting current for both mechanisms (Figure S-1) around the boundary between the KinDR and other kinetic zones. The corresponding sets of parameters are indicated by open and closed circles in Figure 1. However, similarly shaped CVs were obtained for different  $\lambda_{\text{des}}^0$  and  $\kappa$  values of each mechanism to discriminate between the two (Figure S-1). These CVs were not expected for the ACET step alone and had been previously misattributed to the non-concerted mechanism when the adsorption step was not considered in the concerted mechanism [1].

In practice, discrimination of the concerted and non-concerted mechanisms for Case II also requires discrimination between Cases I and II, as discussed in this study. The KinR/KinI, KinDR/KinDI, and KinR'/KinI' zones were expected for Case II, but not for Case I, thereby enabling the identification of Case II. The AR/AI and DO/DI zones were expected for both cases but attributed to Case I because the adsorption of the oxidant was not noticeable in the corresponding CVs. For instance, the underpotential deposition of hydrogen and metals has been studied at low scan rates to observe the AR/AI zone [5]. However, the underpotential deposition process has been attributed to only the ACET step (Case I) [13]. Similarly, the DO/DI zone can be observed for bulk electrodeposition of metals at low scan rates. However, this observation has been attributed to the ACET step only (Case I) [12]. The AR/AI zone or DO/DI zone is accompanied by a manifestation of the KinR/KinI, KinDR/KinDI, or KinR'/KinI' zone for Case II at higher scan rates or lower oxidant concentrations, as previously discussed.

### 3.2.3. Determination of Adsorption Parameters

The characteristic peak and limiting currents of the simulated CVs were consistent with the results of the analytical procedure (Tables S-4 and S-5) for the determination of the adsorption

parameters. For an electrochemically reversible ET,  $\Gamma_s$  can be determined from the peak current of the AR zone, as follows:

$$i_{\text{ET}}^{\text{p}} = \frac{F^2 v A \Gamma_s}{4RT} \quad (20)$$

Alternatively,  $\Gamma_s$  can be determined by a numerical analysis of the characteristic voltammogram of an AR/AI zone with any electrochemical reversibility. For any electrochemical reversibility, the limiting current of the KinDR/KinDI zone includes three adsorption parameters as follows:

$$i_{\text{O}_{\text{ads}}}^{\text{lim}} = F A k_{\text{des}}^0 \beta_0 c_0 \Gamma_s \quad (21)$$

Using  $\Gamma_s$  and  $\beta_0$  obtained from the AR/AI zone, and the peak current from the KinR/KinI zone, respectively,  $k_{\text{des}}^0$  can be determined from Equation 21. The peak current for the electrochemically reversible case is given as follows:

$$i_{\text{ET},\text{O}_{\text{ads}}}^{\text{p}} = \frac{F^2 v A \beta_0 c_0 \Gamma_s}{4RT} \quad (22)$$

The peak current is a function of  $c_0$  and can be discriminated from that of the AR zone (see Equation 20). Notably, the electrode surface was saturated with the oxidant in the AR/AI zone but not the KinDR/KinDI, KinR'/KinI', and KinR/KinI zones. Subsequently, the characteristic currents at the unsaturated surface (Equations 21 and 22) were lowered by  $\beta_0 c_0$  ( $= \rho_0 = 10^{-4}$  in Figure 1); however, the lowered characteristic currents were sufficiently high to follow the order  $i_{\text{ET}}^{\text{p}} < i_{\text{O}_{\text{ads}}}^{\text{lim}} < i_{\text{ET},\text{O}_{\text{ads}}}^{\text{p}}$  when the scan rate was increased for the non-concerted mechanism. The corresponding transitions for the non-concerted mechanism have been indicated by the diagonal arrows across boundaries **3** and **6** in Figure 1B. In addition, the characteristic currents were measurably high when the scan rate and oxidant concentration were appropriately adjusted for the concerted mechanism.

### 3.3. ACET with Reversible Adsorption of Reductant (Case III)

When the reductant is reversibly adsorbed on the electrode surface (Case III), ACET reactions are fundamentally and practically important, as described in the introduction section. The non-concerted mechanism of Case III involves an outer-sphere ET step, as modelled by the Marcus theory [33]. Experimentally, Case III has been previously represented by the adsorption-coupled oxidation of water-soluble ferrocene derivatives at HOPG [31, 32]. The experimental CVs fit very well with the non-concerted mechanism. However, this study demonstrates that both mechanisms yield the same CV because the adsorption of the ferrocene derivatives maintained equilibrium, and the ET steps were chemically reversible [31, 32]. Moreover, Case III has been exemplified by the one-electron reduction of  $O_2$  and  $CO_2$  as the key steps of the multi-electron  $O_2$  [10] and  $CO_2$  [11] reduction reactions, respectively.

#### 3.3.1. Kinetic Zone Diagrams

Kinetic zone diagrams resulting from the simulation of CVs for Case III represent remarkably different voltammetric behaviours between concerted and non-concerted mechanisms (Figures 2A and 2B, respectively), facilitating their discrimination. The zone notations A, D, Kin, R, O, and I are the same as those defined for Case II. In addition, DM and DP indicate the modified- and pure-diffusion-controlled zones, respectively, in the DMR/DMI, ADMR/ADMI, DPR/DPI, and ADPR/ADPI zones. An analytical approach was also used to define the boundaries between the kinetic zones (Tables S-4–S-7).

The diagrams were obtained for a large  $\rho_R$  value of  $10^5$  to yield the adsorption waves for both concerted and non-concerted mechanisms. Diffusion waves were dominant in the non-concerted mechanism with low  $\lambda_{des}^R$  or  $\kappa$  values (Figure 2B), as expected only for the outer-sphere ET step. Under these conditions, the CVs did not confirm the adsorption of the reductant, despite the large  $\rho_R$  value. In the concerted mechanism, the reductant was adsorbed through the ACET step to yield the AR/AI and

DO/DI zones, as expected for Case I. The reductant was also reversibly desorbed to yield other kinetic zones. A large  $\rho_R$  value of  $10^5$  corresponded to a weak adsorption, with a free energy change of  $-28.5$  kJ/mol ( $= -RT\ln\rho_R$  at 298 K). The weak adsorption step justifies the neglection of the partial charge transfer [36, 37] in our model. However, the weak adsorbate can still saturate the electrode surface to yield pre-peaks for both mechanisms at a sufficiently small  $\kappa$ .

The kinetic zone diagrams of Case III (Figure 2) support the analytical assessment of the concerted and non-concerted mechanisms (entry 2, Table 2). The two mechanisms are distinguishable not only when the common adsorption step is kinetically controlled but also when the surface coverage becomes substantial. Accordingly, the concerted and non-concerted mechanisms were equivalent only between a portion of the DO/DI zone (above the dotted line in Figure 2A) and the entire DO/DI zone (Figure 2B). In these regions,  $v_C^0 = v_{OS}^0$  because  $\lambda_{des}^R$  was sufficiently large for equilibrium adsorption and  $\kappa$  was sufficiently large to minimally cover the electrode surface with the adsorbed reductant, that is,  $\Gamma_M \approx \Gamma_s$ . For a smaller  $\kappa$ , the electrode surface was saturated with the adsorbed reductant, that is,  $\Gamma_M \ll \Gamma_s$ , to yield a pair of pre-peaks in the ADMR and ADPR zones. However, these zones were thermodynamically equivalent, as confirmed by the identical CVs. At an even smaller  $\kappa$ , the thermodynamically equivalent DMR and DPR zones resulted in identical CVs, where the pre-peak was exceeded by the diffusion wave.

Notably, the equivalence between the concerted and non-concerted mechanisms of Case III had not been recognised in previous theoretical and experimental studies. The DPR, ADPR, and DO zones were theoretically predicted for the non-concerted mechanism by Wopschall and Shain [18], who assumed an equilibrium adsorption step and an electrochemically reversible outer-sphere ET step. These assumptions imply that identical CVs are expected for concerted mechanisms, as demonstrated in this study. Moreover, the experimental CVs of the water-soluble ferrocene derivatives at HOPG were

analysed assuming a non-concerted mechanism [31, 32]. The experimental CVs were found to be characteristic of the DPR, ADPR, and DO zones based on the equilibrium adsorption step and the electrochemically reversible outer-sphere ET step. Thus, the experimental CVs can also be explained by the concerted mechanisms considered in this study. In either mechanism, the DO zone can be attributed to Case III rather than Cases I or II, because ferrocene derivatives were initially present in the solution [31, 32].

### 3.3.2. Discrimination between Concerted and Non-Concerted Mechanisms

The uniquely shaped CVs resulting from our Case III simulation allow for the identification of the reaction mechanism. For instance, characteristic CVs were expected in the AKinDR/AKinDI zone of the concerted mechanism (Figure 2A) and the DRKin/DIKin and AIDPR zones of the non-concerted mechanisms (Figure 2B). A unique CV of the AKinDR/AKinDI zone has been predicted for the first time in this study. The characteristic limiting current,  $i_{R_{sat}}^{\lim}$ , based on steady-state desorption of the reductant saturated at the electrode surface, can be given by

$$i_{R_{sat}}^{\lim} = FAk_{des}^R \Gamma_s \quad (23)$$

In addition, this study is the first to predict the unique CV of the DRKin/DIKin zone. Here, the reverse peak is broadened and lowered by slow desorption of the reductant, which serves as a measure of the desorption rate constant. The CV of the AIDPR zone has been reported previously [1] and is characterised by the absence of a reverse pre-peak owing to the slow desorption of the reductant. The transition from the ADPR to the AIDPR zone broadens and lowers the reverse pre-peak, thereby enabling the determination of the desorption rate constant. In the AIDPI zone, the forward pre-peak overlaps with the diffusion wave.

Characteristic CVs were also expected in the DMI (Figure 3A), ADMI, and ADPI zones (Figure 3B) owing to irreversible ET steps. In these zones, the electrode surface was saturated with the adsorbed reductant, that is,  $\Gamma_M \ll \Gamma_s$ . Therefore, the CVs of the two mechanisms became distinct when thermodynamic equivalences were not maintained by irreversible ET steps. The unique CVs of the DMI and ADMI zones were observed for the first time in this study, wherein a new concerted mechanism, containing an adsorption step, was considered. The characteristic CV of the ADPI zone has been predicted previously [1].

### *3.4. Electrocatalytic Reduction of Benzyl Chloride (Case IV)*

Our model was extended to discuss the electrocatalytic reduction of benzyl chloride at a Ag electrode as an example of Case IV. The electrocatalytic effect of the Ag electrode on the two-electron reduction of benzyl chloride was supported by CV and surface-enhanced Raman spectroscopy, with specific bands confirmed by DFT [50]. Moreover, the non-concerted mechanism of Case IV was modelled to fit the experimental CVs over a wide range of scan rates from 0.2 to 500 V/s [26]. Recently, a non-concerted mechanism has also been supported by DFT calculations [35]. However, we demonstrate in this study that the experimental CV can also be fitted by considering the concerted mechanism. Equivalence between the two mechanisms is expected, although the common adsorption steps are kinetically controlled; because the ET steps are chemically irreversible (entry 4, Table 2).

#### *3.4.1. Identical Voltammograms with Chemically Irreversible ET Steps*

We considered both concerted and non-concerted mechanisms with chemically irreversible ET steps to simulate identical voltammograms for the reduction of benzyl chloride at the Ag electrode. In the non-concerted mechanism (Figure 4A), the non-adsorbed benzyl chloride (A) was reduced to the

non-adsorbed benzyl radical (B) via the outer-sphere ET step. In addition, the inner-sphere ET step mediated the reduction of adsorbed benzyl chloride ( $A_{ads}$ ) to the adsorbed benzyl radicals ( $B_{ads}$ ), thereby representing Case IV. Similarly, the adsorbed and non-adsorbed forms of the benzyl radicals were reduced to the respective forms of the benzyl anion (C and  $C_{ads}$ ) to represent Case IV. The dynamic adsorption of benzyl chloride and the benzyl radicals and anions was kinetically blocked at sufficiently high scan rates. However, both the adsorbed and non-adsorbed forms of benzyl anions were irreversibly protonated to produce the respective forms of toluene (D and  $D_{ads}$ ). The ET steps were only reductive, rendering the concerted and non-concerted mechanisms equivalent.

We replaced all the inner-sphere and outer-sphere ET steps of the non-concerted mechanism with ACET steps in the concerted mechanism (Figure 4B), which resulted in identical CVs for both mechanisms. Equivalence was maintained at scan rates up to 500 V/s (Figure 5A). The experimental CV fitted well with the CV of the non-concerted mechanism, yielding all the parameters for the adsorption, non-ACET, and chemical reaction steps [26] (Tables S-12 and S-13). These parameters were also used for the adsorption and chemical reaction steps in the concerted mechanism. The standard rate constants of the ACET steps were calculated from those of the non-ACET steps, with the exception of benzyl chloride reduction (Table S-12). The standard rate constant for benzyl chloride reduction was adjusted to fit the CV of the concerted mechanism (Figure 5A) and subsequently, the experimental CV.

In addition, we simulated the current response corresponding to each ET step to obtain identical voltammograms for all the ET steps (Figures 5B and 5C), confirming the equivalence of the ACET and non-ACET steps, as expected from their chemical irreversibility. The second reduction step was fast enough to immediately follow the first, thereby yielding identical voltammograms. Subsequently, the concentrations of all species near and on the electrode surface were also found to be identical in the concerted and non-concerted mechanisms (see Figure S-2 for major species). This indicates that the two

mechanisms cannot be discriminated via non-electrochemical detection of the adsorbates, such as surface spectroscopy [50].

### *3.4.2. Distinct Voltammograms with Chemically Reversible ET Steps*

As a case study, we also simulated the reduction of benzyl chloride via the concerted and non-concerted mechanisms without irreversible chemical steps. We assumed the stability of both the adsorbed and non-adsorbed benzyl anions, although such a strongly basic anion cannot be stable under typical electrochemical conditions. This assumption resulted in remarkably different anodic responses during the reverse potential scan (Figure 5D). This result proves that concerted and non-concerted mechanisms can be discriminated for reduction mechanisms similar to that of benzyl chloride in the absence of irreversible chemical steps. The absence of irreversible chemical steps did not significantly affect the cathodic current response during the forward scan.

We also simulated a voltammogram for each ET step without irreversible chemical steps to distinguish between concerted and non-concerted mechanisms for the first and second oxidation steps. In both mechanisms, the oxidation of the benzyl radical was expected at a significantly higher positive potential than that of the benzyl anion (Figure 5E and 5F, respectively). This ensured that the first and second oxidation steps were resolvable. Moreover, each oxidation step could be identified by the unique shape or peak potential of the corresponding voltammogram during the reverse scan. Diffusion waves with distinct peak potentials were obtained for the outer-sphere and adsorption-coupled oxidation of the non-adsorbed reductant during the reverse scan. Adsorption waves with different peak potentials were obtained when the adsorbed reductant was oxidised via the inner-sphere ET and ACET steps.

### 3.4.3. Other Examples of Case IV

We confirmed the uniqueness of the benzyl chloride reduction at the Ag electrode in comparison with other experimental studies on ACET reactions of Case IV. The kinetics of all adsorption steps were quantitatively characterised for the reduction of benzyl chloride at the Ag electrode [26], for an unambiguous assessment of the ACET mechanism. This was not the case for the oxidation of dopamine [51, 52] or amphiphilic ferrocenes [53-55]. Here, both the reductant and oxidant were adsorbed to yield diffusion and adsorption waves at low and high scan rates, respectively, as expected for Case IV [26]. Adsorption kinetics, however, were fully characterised only for the reduced forms of dopamine and amphiphilic ferrocenes [51, 52, 55]. Moreover, the two-electron oxidation of dopamine at the carbon-fiber electrodes was assumed to proceed via a single step, thereby providing no information about the first oxidation product [51, 52]. Furthermore, desorption of the final product—the *o*-quinone form of dopamine—was too rapid to determine the corresponding desorption rate or equilibrium constant. No thermodynamic or kinetic parameters were obtained for the weak adsorption of amphiphilic ferroceniums, which was examined qualitatively using CV [54, 55] and a quartz crystal microbalance [54].

## 4. Conclusions

In this study, we modelled the concerted and non-concerted mechanisms of ACET reactions with a common adsorption step for the voltammetric discrimination of the two. Our model enables the assessment of experimental voltammograms via both mechanisms, in contrast to previous assessments based on either mechanism [12, 26, 30-32, 47-49]. A voltammetric assessment of the ACET mechanism requires not only a kinetically controlled common adsorption step, as proposed previously [1], but also chemically reversible ET steps. When both requirements are satisfied, characteristic CV shapes or

unique changes therein are expected for each mechanism in Cases II and III. Experimentally, a higher scan rate kinetically limits the adsorption step but increases the background capacitive current and iR drop, which have not been considered in our model. The iR drop can be fully corrected to accurately subtract the capacitive current [38-40] for the quantitative analysis of fast-scan CV [26].

Our model had been previously validated quantitatively [26, 31, 32, 47-49] and in this study, and was applied to the electrocatalytic reduction of benzyl chloride at the Ag electrode as Case IV. To the best of our knowledge, this ACET system is the only example in which the kinetic parameters corresponding to all adsorption steps are available for the unambiguous comparison of concerted and non-concerted mechanisms. The experimental voltammogram of this chemically irreversible ACET reaction was consistent with both mechanisms, quantitatively validating our model. This explains why the exclusive consideration of the non-concerted mechanism in a previous study on this ACET reaction [26], though justifiable for simplicity, was inconclusive. There have been no reports on the experimental demonstration of the voltammetric discrimination between the two mechanisms. In contrast, a distinct CV is expected for each mechanism without irreversible chemical steps, indicating that voltammetric discrimination between the concerted and non-concerted mechanisms will be possible when both the requirements are satisfied.

Overall, we believe that ACET reaction mechanisms can be identified by the analysis of experimental voltammograms using our model. The experimentally identified mechanisms can be useful for verifying the mechanisms predicted by molecular-level theories, such as DFT [28, 29, 34, 35]. The synergy between experimental and theoretical approaches can advance our fundamental understanding of the coupling between ET and the specific adsorption of redox molecules for powerful applications in electrochemistry.

## 5. Acknowledgment

This study was supported by the National Science Foundation (grant number CHE-1904258). D.C.J. and N.K. acknowledge the Arts and Sciences Fellowships from the University of Pittsburgh. K.B. appreciates the DISHA fellowship from the Department of Science and Technology, India. C.A., I.S., and A.O. acknowledge support from UMR 8640 PASTEUR (CNRS, ENS-PSL University, and Sorbonne University). C.A. also thanks Xiamen University for his appointment as a distinguished professor.

## 6. References

- [1] O.V. Klymenko, I. Svir, C. Amatore, Molecular electrochemistry and electrocatalysis: a dynamic view, *Mol. Phys* 112 (2014) 1273–1283. <http://dx.doi.org/10.1080/00268976.2014.890753>
- [2] A. J. Bard, Inner-Sphere Heterogeneous Electrode Reactions. Electrocatalysis and Photocatalysis: The Challenge, *J. Am. Chem. Soc* 132 (2010) 7559–7567. <http://dx.doi.org/10.1021/ja101578m>
- [3] Z.W. Seh, J. Kibsgaard, C.F. Dickens, I.B. Chorkendorff, J.K. Norskov, T.F. Jaramillo, Combining theory and experiment in electrocatalysis: Insights into materials design, *Science* 355 (2017). DOI: 10.1126/science.aad4998
- [4] D. T. Jantz, K. C. Leonard, Characterizing Electrocatalysts with Scanning Electrochemical Microscopy, *Ind. Eng. Chem. Res* 57 (2018) 7431–7440. <http://dx.doi.org/10.1021/acs.iecr.8b00922>
- [5] E. Herrero, L. J. Buller, H. D. Abruña, Underpotential Deposition at Single Crystal Surfaces of Au, Pt, Ag and Other Materials, *Chem. Rev* 101 (2001) 1897–1930. <http://dx.doi.org/10.1021/cr9600363>

[6] M. S. Whittingham, Special Editorial Perspective: Beyond Li-ion Battery Chemistry, *Chem. Rev.* 120 (2020) 6328–6330. <http://dx.doi.org/10.1021/acs.chemrev.0c00438>

[7] J. Heinze, B. A. Frontana-Uribe, S. Ludwigs, Electrochemistry of Conducting Polymers—Persistent Models and New Concepts, *Chem. Rev.* 110 (2010) 4724–4771. <http://dx.doi.org/10.1021/cr900226k>

[8] N. Kurapati, R. M. Buoro, S. Amemiya, Perspective—Beyond the century-long paradigm of hydrogen electrochemistry through the Laviron–Amatore paradox, *J. Electrochem. Soc.* 167 (2020) 146514. <http://dx.doi.org/10.1149/1945-7111/abc840>

[9] P. G. Bruce, M. Y. Saidi, The mechanism of electrointercalation, *J. Electroanal. Chem.* 322 (1992) 93–105. [http://dx.doi.org/10.1016/0022-0728\(92\)80069-G](http://dx.doi.org/10.1016/0022-0728(92)80069-G)

[10] N. Ramaswamy, S. Mukerjee, Alkaline Anion-Exchange Membrane Fuel Cells: Challenges in Electrocatalysis and Interfacial Charge Transfer, *Chem. Rev.* 119 (2019) 11945–11979. <http://dx.doi.org/10.1021/acs.chemrev.9b00157>

[11] Y. Hori, Electrochemical CO<sub>2</sub> reduction on metal electrodes, in *Modern aspects of electrochemistry*: C.G. Vayenas, R.E. White, M.E. Gamboa-Aldeco (Eds.), Vol. 42, Springer, NY, 2008, p. 89–189. [https://doi.org/10.1007/978-0-387-49489-0\\_3](https://doi.org/10.1007/978-0-387-49489-0_3)

[12] I. Atek, S. Maye, H. H. Girault, A. M. Affoune, P. Peljo, Semi-analytical modelling of linear scan voltammetric responses for soluble-insoluble system: The case of metal deposition, *J. Electroanal. Chem.* 818 (2018) 35–43. <http://dx.doi.org/10.1016/j.jelechem.2018.04.021>

[13] M. Yang, R. G. Compton, Voltammetry of Adsorbed Species: Nonideal Interactions Leading to Phase Transitions, *J. Phys. Chem. C* 124 (2020) 18031–18044. <http://dx.doi.org/10.1021/acs.jpcc.0c03791>

[14] S. Martinet, J. Bouteillon, J. P. Caire, Modelling of cyclic voltammograms for two-step metal deposition on an inert electrode with adsorption, *J. Appl. Electrochem* 28 (1998) 819–825. <http://dx.doi.org/10.1023/A:1003424123260>

[15] L. K. Bieniasz, Use of dynamically adaptive grid techniques for the solution of electrochemical kinetic equations: Part 11. Patch-adaptive simulation of example transient experiments described by kinetic models involving simultaneously distributed and localised unknowns, in one-dimensional space geometry, *J. Electroanal. Chem* 527 (2002) 11–20. [https://doi.org/10.1016/S0022-0728\(02\)00812-4](https://doi.org/10.1016/S0022-0728(02)00812-4)

[16] F. G. Chevallier, O. V. Klymenko, L. Jiang, T. G. J. Jones, R. G. Compton, Mathematical modelling and numerical simulation of adsorption processes at microdisk electrodes, *J. Electroanal. Chem* 574 (2005) 217–237. <https://doi.org/10.1016/j.jelechem.2004.07.033>

[17] M. Yang, R. G. Compton, Adsorption processes coupled with mass transport at macro-electrodes: New insights from simulation, *J. Electroanal. Chem* 836 (2019) 68–76. <https://doi.org/10.1016/j.jelechem.2019.01.060>

[18] R. H. Wopschall, I. Shain, Effects of adsorption of electroactive species in stationary electrode polarography, *Anal. Chem* 39 (1967) 1514–1527. <http://dx.doi.org/10.1021/ac50156a018>

[19] A. Molina, J. González, F. Saavedra, L. M. Abrantes, Cyclic reciprocal derivative chronopotentiometry. Applications to the detection and characterisation of adsorption processes, *Electrochim. Acta* 45 (1999) 761–773. [http://dx.doi.org/10.1016/S0013-4686\(99\)00255-8](http://dx.doi.org/10.1016/S0013-4686(99)00255-8)

[20] M. Sluyters-Rehbach, J. H. Sluyters, Some basic views on the influence of reactant adsorption on wave shapes in D.C., A.C. and linear sweep voltammetry, *J. Electroanal. Chem. Interfacial Electrochem* 65 (1975) 831–841. [http://dx.doi.org/10.1016/0368-1874\(75\)85161-6](http://dx.doi.org/10.1016/0368-1874(75)85161-6)

[21] M.-L. Alcaraz, Chronopotentiometric response with programmed current when the reactant and/or product are adsorbed at spherical and planar electrodes, *J. Electroanal. Chem.* 369 (1994) 207–215. [http://dx.doi.org/10.1016/0022-0728\(94\)87100-0](http://dx.doi.org/10.1016/0022-0728(94)87100-0)

[22] S. W. Feldberg, Digital simulation of electrochemical surface boundary phenomena: Multiple electron transfer and adsorption in Electrochemistry, calculations, simulation and instrumentation: J.S. Mattson, H.B. Mark, Jr., H.C. MacDonald, Jr. (Eds.), Marcel Dekker, New York, 1972, p. 185.

[23] E. Laviron, Theoretical study of a simple redox system with adsorption of the reactants on a rotating disk electrode: Part I. The reaction path in the case of a langmuirian adsorption equilibrium, *J. Electroanal. Chem. Interfacial Electrochem.* 124 (1981) 19–33. [http://dx.doi.org/10.1016/S0022-0728\(81\)80282-3](http://dx.doi.org/10.1016/S0022-0728(81)80282-3)

[24] E. Laviron, The use of polarography and cyclic voltammetry for the study of redox systems with adsorption of the reactants. Heterogeneous vs. surface path, *J. Electroanal. Chem.* 382 (1995) 111–127. [http://dx.doi.org/10.1016/0022-0728\(94\)03684-U](http://dx.doi.org/10.1016/0022-0728(94)03684-U)

[25] A. Molina, M.-L. Alcaraz, F. Saavedra, J. González, Application of current reversal chronopotentiometry and cyclic chronopotentiometry to the study of reactant and/or product adsorption at a plane electrode, *Electrochim. Acta* 44 (1998) 1263–1272. [http://dx.doi.org/10.1016/S0013-4686\(98\)00230-8](http://dx.doi.org/10.1016/S0013-4686(98)00230-8)

[26] O.V. Klymenko, O. Buriez, E. Labbe, D. P. Zhan, S. Rondinini, Z. Q. Tian, I. Svir, C. Amatore, Uncovering the Missing Link between Molecular Electrochemistry and Electrocatalysis: Mechanism of the Reduction of Benzyl Chloride at Silver Cathodes, *ChemElectroChem* 1 (2014) 227–240. <http://dx.doi.org/10.1002/celc.201300101>

[27] O.V. Klymenko, I. Svir, C. Amatore, New theoretical insights into the competitive roles of electron transfers involving adsorbed and homogeneous phases, *J. Electroanal. Chem.* 688 (2013) 320–327. <http://dx.doi.org/10.1016/j.jelechem.2012.07.022>

[28] E. Santos, A. Lundin, K. Pötting, P. Quaino, W. Schmickler, Model for the electrocatalysis of hydrogen evolution, *Phys. Rev. B* 79 (2009) 235436. <http://dx.doi.org/10.1103/PhysRevB.79.235436>

[29] L. M. C. Pinto, E. Spohr, P. Quaino, E. Santos, W. Schmickler, Why Silver Deposition is so fast: Solving the Enigma of Metal Deposition, *Angew. Chem. Int. Ed.* 52 (2013) 7883–7885. <http://dx.doi.org/10.1002/anie.201301998>

[30] T. Shinagawa, A.T. Garcia-Esparza, K. Takanabe, Insight on Tafel slopes from a microkinetic analysis of aqueous electrocatalysis for energy conversion, *Sci. Rep.* 5 (2015) 13801. <http://dx.doi.org/10.1038/srep13801>

[31] N. Kurapati, P. Pathirathna, R. Chen, S. Amemiya, Voltammetric Measurement of Adsorption Isotherm for Ferrocene Derivatives on Highly Oriented Pyrolytic Graphite, *Anal. Chem.* 90 (2018) 13632–13639. <http://dx.doi.org/10.1021/acs.analchem.8b03883>

[32] N. Kurapati, P. Pathirathna, C. J. Ziegler, S. Amemiya, Adsorption and Electron-Transfer Mechanisms of Ferrocene Carboxylates and Sulfonates at Highly Oriented Pyrolytic Graphite, *ChemElectroChem* 6 (2019) 5651–5660. <http://dx.doi.org/10.1002/celc.201901664>

[33] R. A. Marcus, On the Theory of Electron-Transfer Reactions. VI. Unified Treatment for Homogeneous and Electrode Reactions, *J. Chem. Phys.* 43 (1965) 679–701. <http://dx.doi.org/10.1063/1.1696792>

[34] W. Schmickler, Electron and ion transfer reactions on metal electrodes, *Electrochim. Acta* 41 (1996) 2329–2338. [http://dx.doi.org/10.1016/0013-4686\(96\)00063-1](http://dx.doi.org/10.1016/0013-4686(96)00063-1)

[35] Y.-L. Chen, T.-W. Weng, Z.-Y. Cai, H. Shi, T.-R. Wu, D.-Y. Wu, A. Oleinick, I. Svir, B.-W. Mao, C. Amatore, Z.-Q. Tian, A DFT and SERS study of synergistic roles of thermodynamics and kinetics during the electrocatalytic reduction of benzyl chloride at silver cathodes, *J. Electroanal. Chem.* 914 (2022) 116267. <http://dx.doi.org/10.1016/j.jelechem.2022.116267>

[36] W. Schmickler, R. Guidelli, The partial charge transfer, *Electrochim. Acta* 127 (2014) 489–505. <http://dx.doi.org/10.1016/j.electacta.2014.02.057>

[37] A. Lasia, The Origin of the Constant Phase Element, *J. Phys. Chem. Lett.* 13 (2022) 580–589. <http://dx.doi.org/10.1021/acs.jpclett.1c03782>

[38] J. C. Imbeaux, J. M. Savéant, Linear sweep voltammetry. Effect of uncompensated cell resistance and double layer charging on polarization curves, *J. Electroanal. Chem. Interfacial Electrochem* 28 (1970) 325–338. [http://dx.doi.org/10.1016/S0022-0728\(70\)80127-9](http://dx.doi.org/10.1016/S0022-0728(70)80127-9)

[39] J. C. Imbeaux, J. M. Savéant, Linear sweep voltammetry. Ohmic drop and chemical polarization, *J. Electroanal. Chem. Interfacial Electrochem* 31 (1971) 183–192. [http://dx.doi.org/10.1016/S0022-0728\(71\)80056-6](http://dx.doi.org/10.1016/S0022-0728(71)80056-6)

[40] C. P. Andrieux, D. Garreau, P. Hapiot, J. Pinson, J. M. Savéant, Fast sweep cyclic voltammetry at ultra-microelectrodes: Evaluation of the method for fast electron-transfer kinetic measurements, *J. Electroanal. Chem. Interfacial Electrochem* 243 (1988) 321–335. [http://dx.doi.org/10.1016/0022-0728\(88\)80037-8](http://dx.doi.org/10.1016/0022-0728(88)80037-8)

[41] A. Oleinick, I. Svir, C. Amatore, A few key theoretical issues of importance in modern molecular electrochemistry, *Curr. Opin. Electrochem.* 13 (2019) 33–39. <http://dx.doi.org/10.1016/j.coelec.2018.10.008>

[42] A. Oleinick, I. Svir, C. Amatore, Transient cyclic voltammetry: new theoretical challenges to bring up to date a famous electrochemical lady, *J. Solid State Electrochem* 24 (2020) 2023–2025. <http://dx.doi.org/10.1007/s10008-020-04553-x>

[43] J. M. Pingarrón, J. Labuda, J. Barek, C. M. A. Brett, M. F. Camões, M. Fojta, D. B. Hibbert, Terminology of electrochemical methods of analysis (IUPAC Recommendations 2019), *Pure Appl. Chem* 92 (2020) 641–694. <http://dx.doi.org/10.1515/pac-2018-0109>

[44] C. Amatore, O. Klymenko, I. Svir, A new strategy for simulation of electrochemical mechanisms involving acute reaction fronts in solution: Principle, *Electrochem. Commun* 12 (2010) 1170–1173. <http://dx.doi.org/10.1016/j.elecom.2010.06.009>

[45] A. J. Bard, L. R. Faulkner, H. S. White, *Electrochemical Methods: Fundamentals and Applications*, 3rd ed., John Wiley & Sons, New York, 2022, p. 262.

[46] A. J. Bard, L.R. Faulkner, H.S. White, *Electrochemical Methods: Fundamentals and Applications*, 3rd ed., John Wiley & Sons, New York, 2022 p. 317.

[47] Z. Liang, H. S. Ahn, A. J. Bard, A Study of the Mechanism of the Hydrogen Evolution Reaction on Nickel by Surface Interrogation Scanning Electrochemical Microscopy, *J. Am. Chem. Soc* 139 (2017) 4854–4858. <http://dx.doi.org/10.1021/jacs.7b00279>

[48] M. A. Bhat, N. Nioradze, J. Kim, S. Amemiya, A. J. Bard, In situ detection of the adsorbed Fe(II) intermediate and the mechanism of magnetite electrodeposition by scanning electrochemical microscopy, *J. Am. Chem. Soc* 139 (2017) 15891–15899. <http://dx.doi.org/10.1021/jacs.7b08835>

[49] R. Chen, A. M. Najarian, N. Kurapati, R. J. Balla, A. Oleinick, I. Svir, C. Amatore, R. L. McCreery, S. Amemiya, Self-Inhibitory Electron Transfer of the Co(III)/Co(II)-Complex Redox Couple at Pristine Carbon Electrode, *Anal. Chem* 90 (2018) 11115–11123. <http://dx.doi.org/10.1021/acs.analchem.8b03023>

[50] A. Wang, Y.-F. Huang, U. K. Sur, D.-Y. Wu, B. Ren, S. Rondinini, C. Amatore, Z.-Q. Tian, In Situ Identification of Intermediates of Benzyl Chloride Reduction at a Silver Electrode by SERS Coupled with DFT Calculations, *J. Am. Chem. Soc.* 132 (2010) 9534–9536. <http://dx.doi.org/10.1021/ja1024639>

[51] B. D. Bath, D. J. Michael, B. J. Trafton, J. D. Joseph, P. L. Runnels, R. M. Wightman, Subsecond Adsorption and Desorption of Dopamine at Carbon-Fiber Microelectrodes, *Anal. Chem.* 72 (2000) 5994–6002. <http://dx.doi.org/10.1021/ac000849y>

[52] B. D. Bath, H. B. Martin, R. M. Wightman, M. R. Anderson, Dopamine Adsorption at Surface Modified Carbon-Fiber Electrodes, *Langmuir* 17 (2001) 7032–7039. <http://dx.doi.org/10.1021/la0106844>

[53] T. Saji, K. Hoshino, S. Aoyagui, Reversible formation and disruption of micelles by control of the redox state of the head group, *J. Am. Chem. Soc.* 107 (1985) 6865–6868. <http://dx.doi.org/10.1021/ja00310a020>

[54] J. J. Donohue, D. A. Buttry, Adsorption and micellization influence the electrochemistry of redox surfactants derived from ferrocene, *Langmuir* 5 (1989) 671–678. <http://dx.doi.org/10.1021/la00087a020>

[55] W. F. Peng, D. L. Zhou, J. F. Rusling, Adsorption-Desorption Dynamics of Amphiphilic Ferrocenes on Electrodes Studied by Flow Voltammetry, *J. Phys. Chem.* 99 (1995) 6986–6993. <http://dx.doi.org/10.1021/j100018a035>

## Figure Captions

**Figure 1.** Kinetic zone diagrams of (A) concerted and (B) non-concerted mechanisms in Case II with  $\rho_0 = 10^{-4}$ . Zone notations: D stands for diffusion-controlled behaviour; A for adsorptive; R (or O) for reversible (or ordinary); and I for irreversible. Kin indicates that the forward (or reverse) wave is kinetically controlled by the adsorption (or desorption) step. The two CV shapes corresponding to the reversible and irreversible ET steps have been indicated for each zone by plotting the forward wave upwards and the reverse wave downwards. COMSOL was used to simulate the CVs. The direction and length of the diagonal and lateral arrows indicate the transitions between the kinetic zones at a ten-fold scan rate and one-tenth of the oxidant concentration, respectively. Boundaries **2**, **4**, and **5** depend on  $\rho_0$  (Table S-6). The closed and open circles indicate the parameters used for the simulation of the CVs in Figure S-1.

**Figure 2.** Kinetic zone diagrams of (A) concerted and (B) non-concerted mechanisms in Case III with  $\rho_R = 10^5$ . Zone notations: D stands for diffusion-controlled behaviour; A for adsorptive; R (or O) for reversible (or ordinary); and I for irreversible. Kin indicates that the forward (or reverse) wave is kinetically controlled by the adsorption (or desorption) step; DM and DP stand for modified- and pure-diffusion-controlled, respectively, in the DMR, ADMR, DPR, ADPR, and AIDPR/AIDPI zones. The two CV shapes with the reversible and irreversible ET steps have been indicated for each zone except DMI, ADMI, DPI, and ADPI (see Figure 3) by plotting the forward wave upwards and the reverse wave downwards. COMSOL was used to simulate the CVs. Boundaries **7** and **8** depend on  $\rho_R$  (Table S-7).

**Figure 3.** Comparisons of the CVs based on the concerted and non-concerted mechanisms between (A) the DMI and DPI zones and (B) the ADMI and ADPI zones in Case III with  $\lambda_{\text{des}}^0 = 10^6$  and  $\rho_R = 10^5$ . Zone notations: A stands for adsorption-controlled behaviour; I stands for irreversible; and DM and DP stand for modified- and pure-diffusion-controlled, respectively, to define the DMI, ADMI, DPI, and ADPI zones. The DMI, DPI, ADMI, and ADPI zones are the electrochemically irreversible counterparts of the DMR, DPR, ADMR, and ADPR zones, respectively, in Figure 2. The normalised current is defined by Equation 9. The potential is defined against  $E_{\text{OS}}^{0',0}$ . The respective mechanisms employed (A)  $v_{\text{OS}}^0 = 2 \times 10^{-2}$  and  $v_C^0 = 10^3$ , in addition to  $\kappa = 10^{-3}$  and (B)  $v_{\text{OS}}^0 = 1.5 \times 10^{-3}$  and  $v_C^0 = 10^2$  in addition to  $\kappa = 1$ . COMSOL was used to simulate the CVs.

**Figure 4.** (A) Non-concerted and (B) concerted mechanisms for the adsorption-coupled reduction of benzyl chloride (A and  $A_{\text{ads}}$ ) at a Ag electrode followed by the reduction of the benzyl radical (B and  $B_{\text{ads}}$ ) and the irreversible protonation of the benzyl anion (C and  $C_{\text{ads}}$ ) to toluene (D and  $D_{\text{ads}}$ ). The arrows indicate the outer-sphere ET (red) and equivalent ACET steps (green), as well as the inner-sphere ET (blue) and equivalent ACET steps (yellow). The adsorptive and chemical steps have been indicated by black and purple arrows, respectively.

**Figure 5.** CVs simulated for the reduction of benzyl chloride at a Ag electrode via the non-concerted and concerted mechanisms (A–C) with and (D–F) without the reaction of the benzyl anion with toluene. The current was defined for the concerted and non-concerted mechanisms by Equations S-26 and S-27, respectively, and normalised using Equation 9 to obtain Equations S-28 and S-29. The potential was defined against a saturated calomel electrode in ref. 26. The resultant normalised current is based on (A and D) the entire reaction, (B and E) the reduction of benzyl chloride (A and  $A_{\text{ads}}$ ) to the benzyl radical

(B and  $B_{ads}$ ), and (C and F) the reduction of the benzyl radical to the benzyl anion (C and  $C_{ads}$ ). COMSOL was used to simulate the CVs.

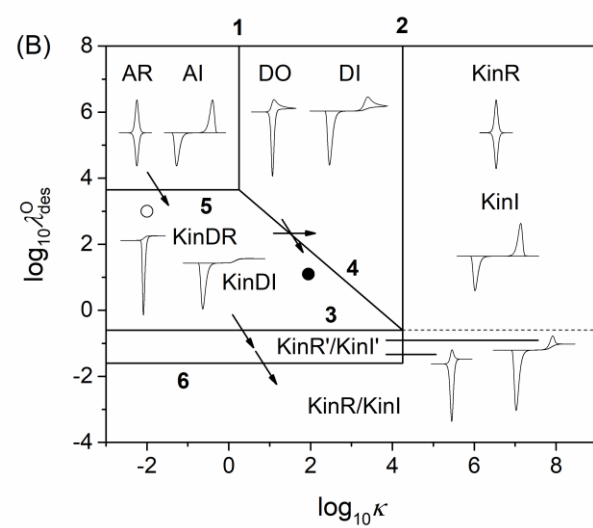
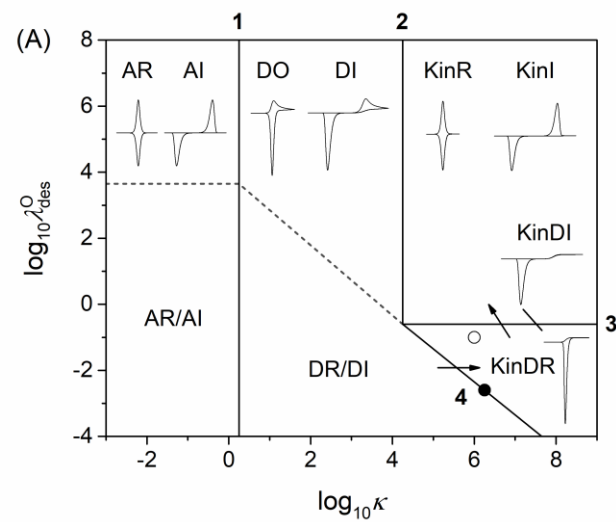


**Figure 1**

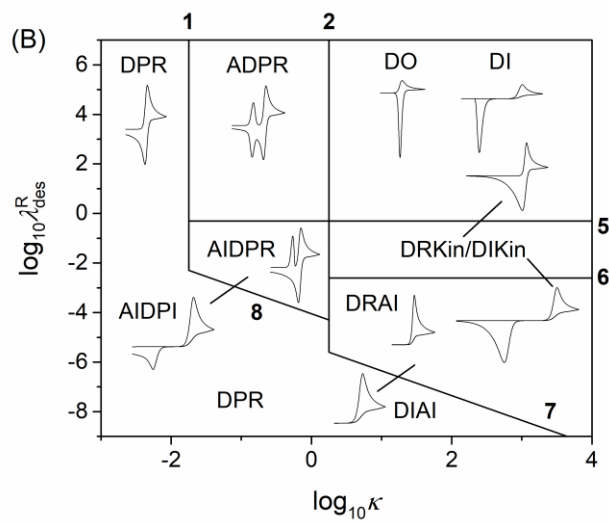
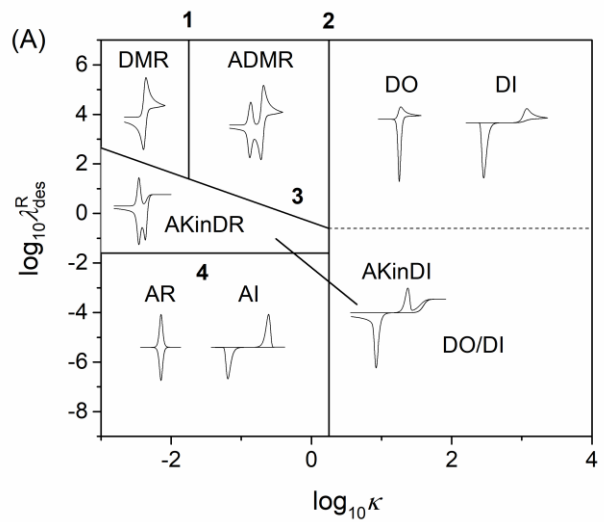


**Figure 2**

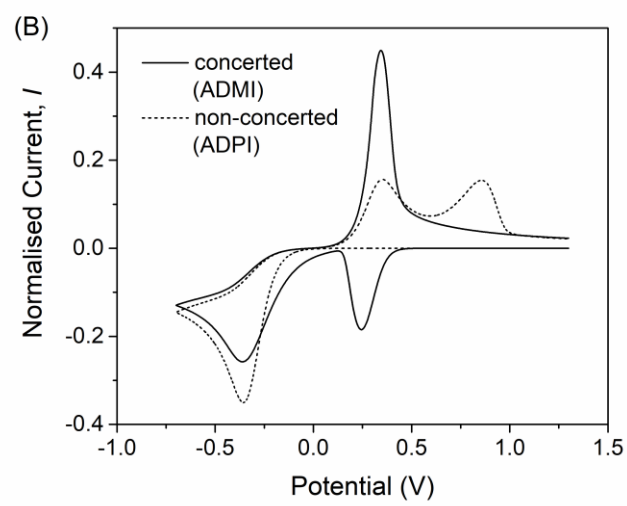
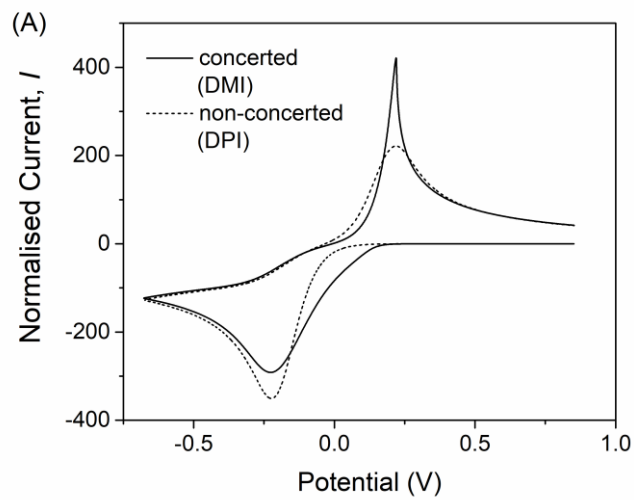


**Figure 3**

(A) Non-concerted Mechanism      (B) Concerted Mechanism

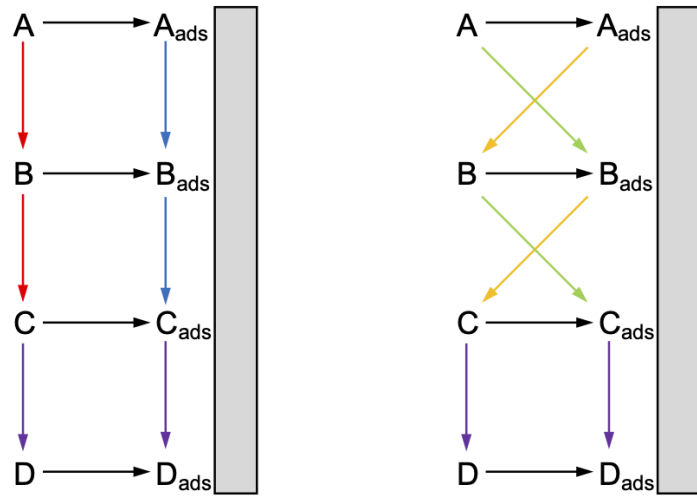
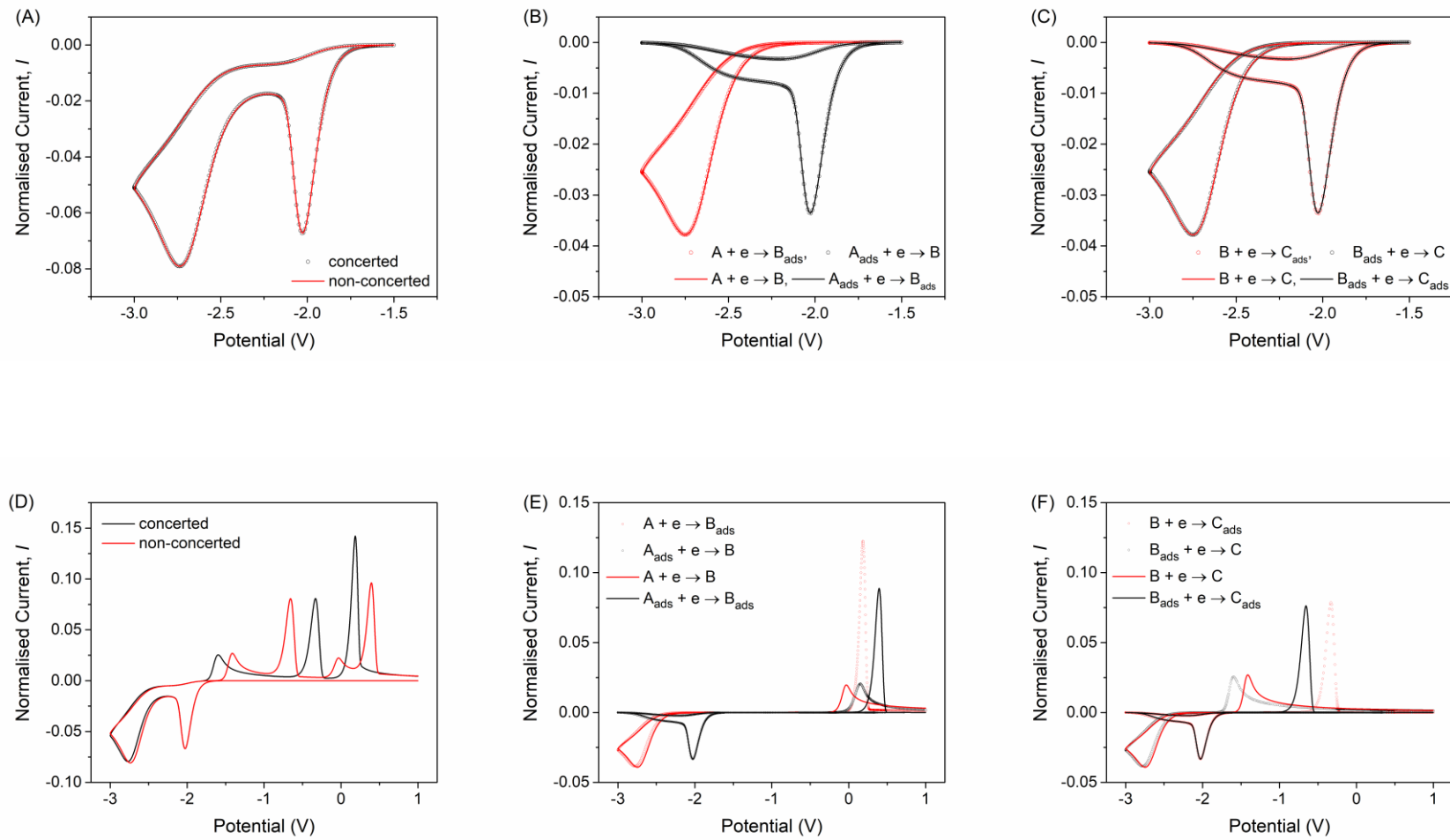


Figure 4



**Figure 5**

**Table 1. Concerted and non-concerted mechanisms of ACET reactions with different adsorption properties of the redox couples**

Case	I	II	III	IV
Adsorption of oxidant	none	reversible	none	reversible
Adsorption of reductant	irreversible	irreversible	reversible	reversible
Concerted mechanism <sup>a,b</sup>				
Non-concerted mechanism <sup>a,c</sup>	none			

<sup>a</sup> The black arrows indicate the reversibility of the adsorption process; <sup>b</sup> the green and yellow arrows the one-electron ACET steps;

and <sup>c</sup> the red and blue arrows the one-electron outer-sphere and inner-sphere ET steps, respectively.

**Table 2. ET equivalence between concerted and non-concerted mechanisms.**

Case	ET equivalence	Requirements	
		Adsorbed species <sup>b</sup>	ET <sup>c</sup>
II	$v_C^0 = v_{IS}^{O_{ads}}$	oxidant	oxidation
III	$v_C^0 = v_{OS}^{O^a}$	reductant	reduction
IV	$v_C^0 = v_{IS}^{O_{ads}}$ and $v_C^{O_{ads}} = v_{OS}^{O^a}$	oxidant	oxidation
	$v_C^0 = v_{OS}^{O^a}$ and $v_C^{O_{ads}} = v_{IS}^{O_{ads}}$	reductant	reduction
	$v_C^0 = v_{IS}^{O_{ads}} = v_C^{O_{ads}} = v_{OS}^{O^a}$	both	—

<sup>a</sup>  $\Gamma_M \approx \Gamma_s$  is required in Equations 13 and 14. <sup>b</sup> Equilibrium. <sup>c</sup> Unidirectional.